Results in Physics 12 (2019) 1628–1644

Contents lists available at ScienceDirect

Results in Physics

journal homepage: www.elsevier.com/locate/rinp

Investigating the structural modifications in LaAlYbCuO

M.E. Emetere[a,d,*], T.W.P. Seadira[b], M. Madhuku[c], M.E. Segale[b]

[a] Department of Physics, Covenant University, Canaan Land, P.M.B 1023, Ota, Nigeria
[b] Department of Civil and Chemical Engineering, University of South Africa, South Africa
[c] NRF-iThemba LABS, Johannesburg, South Africa
[d] Department of Mechanical Engineering Science, University of Johannesburg, South Africa

ARTICLE INFO

Keywords:
Cuprates
Superconductor
Structure
Lanthanum
Structural modulation

ABSTRACT

In this research, we seek a new superconducting candidate LaAlYbCuO based on the need to improve upon the lanthanum cuprates framework. LaAlYbCuO high temperature superconductor was prepared by standard solid-state reaction. The characterization was done by the X-ray powder diffraction technique, Scanning Electron Microscopy (SEM) and Rutherford Backscattering Spectrometry (RBS). The analysis of the images was done using Match, Vesta, SRIM, CERN-Root, OMDAQ and Gwydion software. The XRD refinements show that LAYbCO has orthorhombic structure with unit cell as a = 3.865 Å, b = 3.865 Å, c = 19.887 Å. The specimen had theta correction of 0.19891°. The ratio of electron to phonon production in LAYbCO is approximately 999:1. However, this does not rule-out the possibility of electron-phonon interaction. The elemental composition of LAYbCO is given as $La_{1.35}Al_{3.97}$ $Yb_{6.80}Cu_{6.80}O_{15}$ at Q-factor – 0.033, Chi-square – 0.6057 and dMax – 173. The new LAYbCO framework showed high chemical homogeneity. It was discovered that natural inclination of the atomic structure is quite important for structural interpretations.

Introduction

Axe and Crawford [1] reported that Lanthanum based superconductor has subtle structural modifications due to the several closely related distortions in its structures. The distortions sometimes enable the extraordinary enhancement of its electronic properties under compression [2]. Also, the structural modification of lanthanum superconductor makes it undergo soft mode phase transformation and structural phase transitions. The structural phase transitions in lanthanum are sometimes evidence of anomalies in its structure.

It is still unclear how positively or negatively the inherent distortions affect the superconductivity in lanthanum superconductor. Hence, this research seeks for new candidate of the lanthanum superconductor that have predefined polymorphic forms for further research. The selected elements of the new lanthanum superconductor are envisaged due to its collective transport behavior through the electronic potential of the sample [3]. The ultimate goal of the research is to seek lanthanum framework that has higher critical temperature Tc and potentially broader ranges of stability [4]. The composition of the new lanthanum framework (LAYbCO) is made-up of lanthanum, aluminum, ytterbium, copper and oxygen. Aluminum was chosen because of its peculiar resistance peak and phase slips in the superconducting state [5]. Ytterbium was chosen because it stabilizes the tilted structures [6], promotes larger tilts at low temperatures, and eliminates metastable coexistence at low temperatures [7]. This proposition is to initiate a driving force due to its polymorphic forms. The polymorphic forms in the superconductor have significant influence on its critical temperature as presented in Table 1. LaH_x has high critical temperature i.e. compared to other lanthanum superconductors. It is suggested that the introduction of a clathrate structure (hydrides) into the lanthanum superconductor will have significant influence on the critical temperature [8]. However, the degree of instability in the proposed compound is not known.

In this research paper, the structure of the new lanthanum-superconducting framework was proposed and synthesized. The characterization of the emerging samples was done using x-ray powder diffrac-

* Corresponding author at: Department of Physics, Covenant University, Canaan Land, P.M.B 1023, Ota, Nigeria.
E-mail address: emetere@yahoo.com (M.E. Emetere).

https://doi.org/10.1016/j.rinp.2019.01.058
Received 10 October 2018; Received in revised form 22 January 2019; Accepted 22 January 2019
Available online 25 January 2019

Table 1
Critical temperatures of lanthanum superconductors.

Lanthanum superconductors	Critical Temperature (K)	Reference
$La_{2x}Ba_xCuO_4$	30	[12]
$La_{2-x}Sr_xCuO_4$	38	[9]
$La_{1.48}Nd_{0.4}Sr_{0.12}CuO_4$	22	[9]
LaFePO	4	[10]
LaNiPO	3	[10]
$LaFeAsO_{1-x}F_x$	26	[10]
$La_{1.85}Sr_{0.15}CuO_4$	38	[12]
La_2CuO_y	30	[11]
LaH_x	215	[8]
$La_{2-x}Sr_xNiO_4$	40	[13]

tion, scanning electron microscopy and Rutherford backscattering spectrometry. The in-depth analysis of the proposed structure was done using proven software and codes.

Material and methods

The polycrystalline samples of LaAlYbCuO were prepared by solid state synthesis method, using high purity chemicals of La $(NO_3)_3$ 0.6 H_2O, Al $(NO_3)_3$ 0.6 H_2O, $Yb(NO_3)_3{\cdot}9H_2O$, $Cu(NO_3)_2{\cdot}3H_2O$, citric acid and Ethylene Glycol (Aldrich > 99.9%). Stoichiometric amounts of the chemicals were weighed using an electronic balance. The chemicals were mixed individually in 10 ml of distilled water inside different beakers. All the chemicals were mixed in a 100 ml beaker. The mixture was stirred at 90 °C on a digital mixer (700 rpm) for thirty minutes. The polyesterification of the homogenous blue solution was done at 350 °C for 2 h. The resulting product was thoroughly mixed and grinded using an agate mortar. The product was calcine for 5 h in air at 800 °C to give a dark ash powder. The powder was grinded the second time using the agate mortar. After grinding, the powder was formed into cylindrical pellets under a pressure of 13 kN at room temperature for 7 min. The pellet was sintered at 850 °C for 60 min (1 h) and cooled in air at room temperature. The pellet was sintered the second time at 850 °C for 16 h. The sample was allowed to cool in air at room temperature.

Phase analysis of the sample was done at room temperature using X-ray diffraction(XRD) on a Siemens D8-Advance powder diffractometer at Cu-Ka radiation (λ = 1.5418°A) with an angle step of 0.021. The phase identification was performed using Match software. Microstructural examinations of the samples were done on a scanning electron microscopy (SEM). The microstructural size changes and lattice stability of the SEM images was done using the Gwydion software. The in-depth analysis of the bond and structural complication of the SEM images was demonstrated using the Vesta software. The CERN-Root software was used for graphical plots. Elemental or compositional analysis of the sample was done using Rutherford backscattering spectrometry. The analysis was done using the SRIM and OMDAQ software.

Results and discussion

The orthorhombic structure shown in Fig. 1 has its highest peak at 2θ = 32.58°. The properties at the highest peak are (2 2 2) plane with a theta correction of 0.19891°. The peak of the phases range is within 9.843° – 91.250°. The reflections of the orthorhombic phase are shown in Fig. 1. The phase analysis based on available database is shown in Table 2. Also, the phase identification is presented in Fig. 2. The characterization of the peaks shows that the peak intensity belonging to the selected phases in Table 2 is 62.90% while the unidentified peak intensity is 37.10% (Table 3). The unidentified peaks in Table 3 may be associated with impurities in compounds, non-superconducting impurity phase or earth-based superconducting phases [14,15]. Basically, the crystal structure of LAYbCO compound is comprised of LaO/CuO2/LaO/CuO2/YbO/AlO layers. The Vesta software was used to reassess the X-ray dispersion coefficient of the elements as shown in Table 4. It can be seen from the μ/ρ factor that the peak residual is more associated with the earth-based superconducting phases. Also, the unidentified

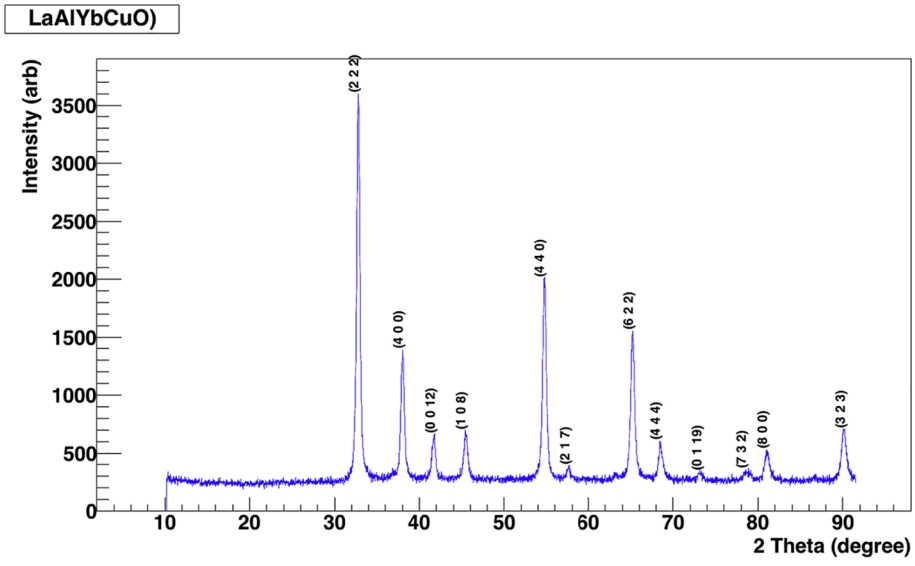

Fig. 1. XRD patterns of LaAlYbCuO.

Table 2
Matched Phases of sample with existing crystal phase database.

Index	Amount	Name	Formula sum	Space Group	Crystal System	References
A	41.0	Cu3 Te O6	Cu3 Te O6	I a 3	cubic	[18]
B	25.4	La4 Ni3 O8	La4 Ni3 O8	I 4/m m m	Tetragonal	[19]
C	20.6	Al Li O2	Al Li O2	R 3 m	Triagonal	[20]
D	13.0	Ir Yb	Ir Yb	P m 3 m	Cubic	[21]

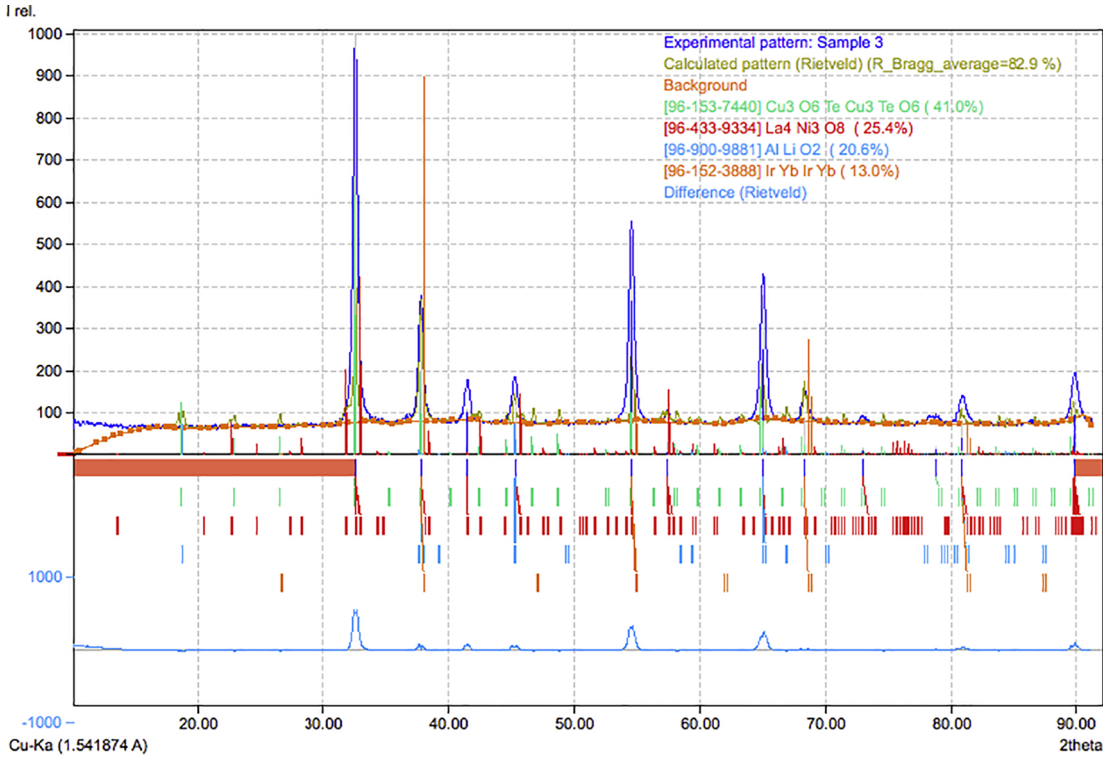

Fig. 2. XRD phase identification of LaAlYbCuO.

Table 3
Reflection Peak characterization.

Peak Data	Counts	Amount
Overall peak intensity	5628	100.00%
Peak intensity belonging to selected phases	3540	62.90%
Unidentified peak intensity	2088	37.10%

Table 4
X-ray dispersion coefficients for λ = 0.1540598 nm.

Element	f'	f''	f_NT	μ/ρ (cm^2/g)
La:	−1.60213E+00	9.01977E+00	−1.28310E−02	3.44076E+02
Cu:	−2.02777E+00	5.83511E−01	−7.26020E−03	5.01091E+01
O:	4.77540E−02	3.20501E−02	−2.19440E−03	1.09804E+01
Al:	2.10520E−01	2.45570E−01	−3.43610E−03	4.85077E+01
Yb:	−7.30624E+00	4.39526E+00	−1.55340E−02	1.38253E+02

peaks may possibly originate from non-superconducting impurity phase [17–19] i.e. from the information on the XRD image and 'μ/ρ' term in Table 4. From the existing database presented in Table 2, the unit cell of the sample has an average value of a = 4.91 Å, c = 20.16 Å. However, the Vesta software gave unit cell of the LAYbCO compound as a = 3.865 Å, b = 3.865 Å, c = 19.887 Å.

Microstructural examinations of the LAYbCO compound using scanning electron microscopy (SEM) show that the granular morphology of the images at localized sites are slightly dissimilar with significant porosity and dense microstructure (Fig. 3a–c). Fig. 3a has micron marker of 100 μm and magnification of 180, Fig. 3b has micron marker of 100 μm and magnification of 230, and Fig. 3c has micron marker of 50 μm and magnification of 330. More significant analysis was carried-out on the Gwydion software.

The atomic lattice structure of the compound can be obtained via SEM as presented in Fig. 4 and it is clearly visible. Fig. 4a, c, e is the 2D lattice structure while Fig. 4b, d, f is the 3D lattice structure. The first observation in Fig. 4a is that the sample do not have either a perfect square lattice structure [16] eor a triangular lattice structure [16]. The XRD and SEM analyses shows that the compounds have an

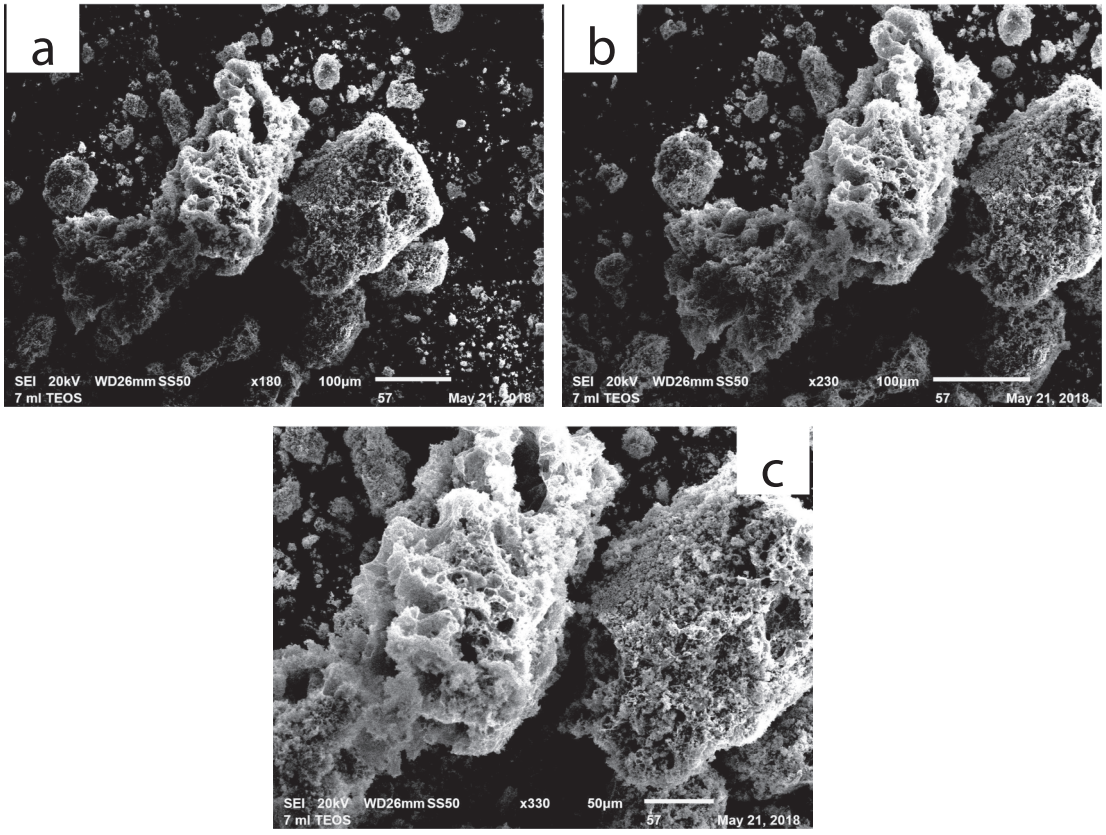

Fig. 3. SEM images of LaAlYbCuO.

orthorhombic lattice. The lattice space observed is unique and it describes region susceptible to lattice displacement. The 3D lattice representation (Fig. 4b) shows an anomalous enhancement of the orthorhombic strain due to differing lattice stiffnesses (blue spaces). The second SEM image (Fig. 4c) of the same sample (i.e. at different micromarker and magnification) show the evidence of lattice mismatch at room temperature. Lattice mismatch is not common to lanthanum superconductor. In this case, it is proof that the CuO_2 plane is under chemical pressure. Studies have shown that chemical pressure due to mismatch in the sub-lattices has significant influence on the transition temperature [22,23]. The orthorhombic strain (blue region in Fig. 4d) further shows the possibility of lattice mismatch at room temperature without applying external pressure. Fig. 4e & f connote that the b-axis may be larger than the a-axis without O(1) site being fully occupied. Hence, the new LAYbCO framework has successfully mitigated against the assertions of compound instability due to distortions.

Fig. 5 gives information on the nature of the ionic mobility. The ionic pattern within the atomic lattice (shown in Fig. 5a) were reproduced as shown in Fig. 5b (i.e. using the Gwydion software). The ionic bond b_1 shows La cation residing between double layers of the copper oxygen with 8-fold coordination while ionic bond b_2 shows the double CuO_2 layers oriented in the (2 2 2) plane as shown in the XRD measurements. The planar structure was constructed in Fig. 5b, d & f to further understand the ionic pattern shown in Fig. 4a, c & e. The ionic distribution shown in Fig. 5a is along the ab-axis (Fig. 5b). Fig. 5c and e lies on the ab-axis and c-axis as shown in Fig. 5d and f respectively. This result supports the assertion made earlier on the possibility of an occurrence of lattice mismatch at room temperature without applying chemical pressure. The full analysis of selected interatomic distances (Å) and bond angles are shown in Table 5.

From the interatomic distance on the z-axis, component of the b_1 bond has affirmed that the double layers of copper and oxygen reside within the 4e site. Also, it can be observed that most O (i.e. O(1) and O (2)) participates in Wyckoff positions 4e site. O(1) lie in the 8 g site and is not fully occupied. The cations of La and Al reside within the same Wyckoff position and z-axis. Hence YbO plane may likely be in the Wyckoff positions 4e site as O. The constituent of the coagulation of ions e.g. b_3 in Fig. 3a have been verified i.e. the YbO/Cu(1)O(3)2/La1/Cu(2)O(4)/LaAl layers. The bond angles in the 4e and 8 g Wyckoff positions are illustrated in Table 6. It can be inferred that the interatomic bond angles in the Al site decrease along the a-axis and fluctuate along the b-axis. It observed that the decrease or increase of coherence length along the c-axis depends on the YbO site (as shown in Table 6).

The SEM images were examined by cropping the images into four parts. Each of the cropped images were labeled section 1–4. The details in the interatomic distance (z) and its corresponding size (p) were extracted and presented as shown in Fig. 6. Fig. 6a & b are extractions from Fig. 3a. Fig. 6c & d are extractions from Fig. 3b. Fig. 6e & f are

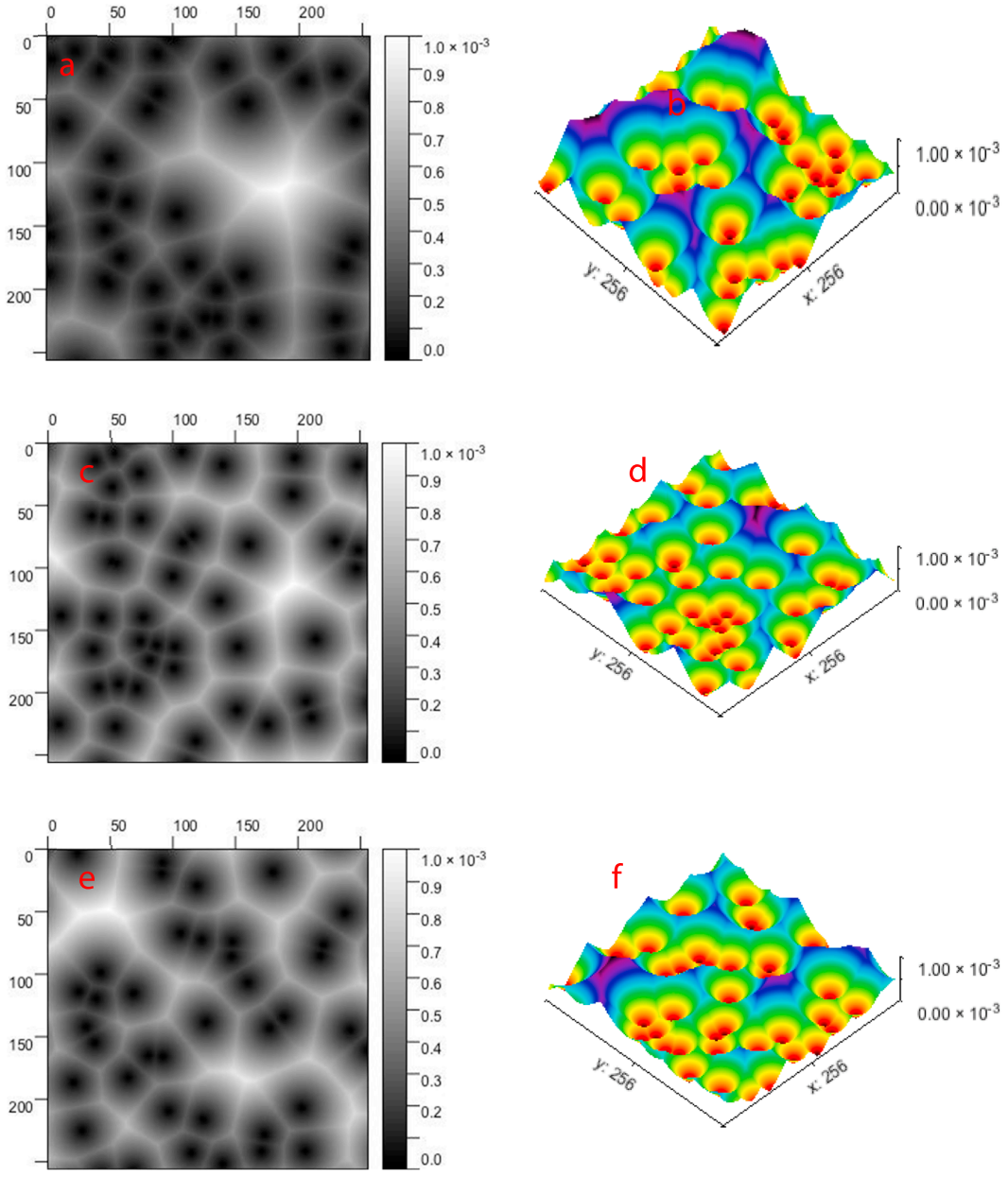

Fig. 4. Atomic lattice structure in LAYbCO.

extractions from Fig. 3c. The background of the SEM image is believed to be the CuO_2 plane. At longer interatomic distance, the interatomic size decreases. Secondly, the varying images (both on the whole sample and the (background) CuO_2 plane) are evidence that CuO_2 plane plays a salient role in local lattice mismatch even at room temperature. Fig. 6b, d, & f show three fundamental characteristics of the CuO_2 plane in LAYbCO framework. First, the scattered peaks (Fig. 6b) presents a wide interatomic distances within the plane that makes it susceptible to out-of-plane interaction. Second, sharp coherence peaks (Fig. 6d & f) shed more light on a dynamic atomic-scale mechanism in CuO_2 plane that determines random gap disorder associated with the dopant atoms [24]. The trigger point of the dynamic atomic-scale mechanism in CuO_2 plane is still unknown. However, it is observed that the background (CuO_2) shown in Fig. 6 b, d & f had no significant influence on the LAYbCO sample (Fig. 6a, b & c). This observation may be peculiar to lanthanum superconductors. Hence, unlike the Yttrium super-conductors [15,25,26], the mechanism of the lanthanum super-conductors may not significantly depend on the copper-oxide as its

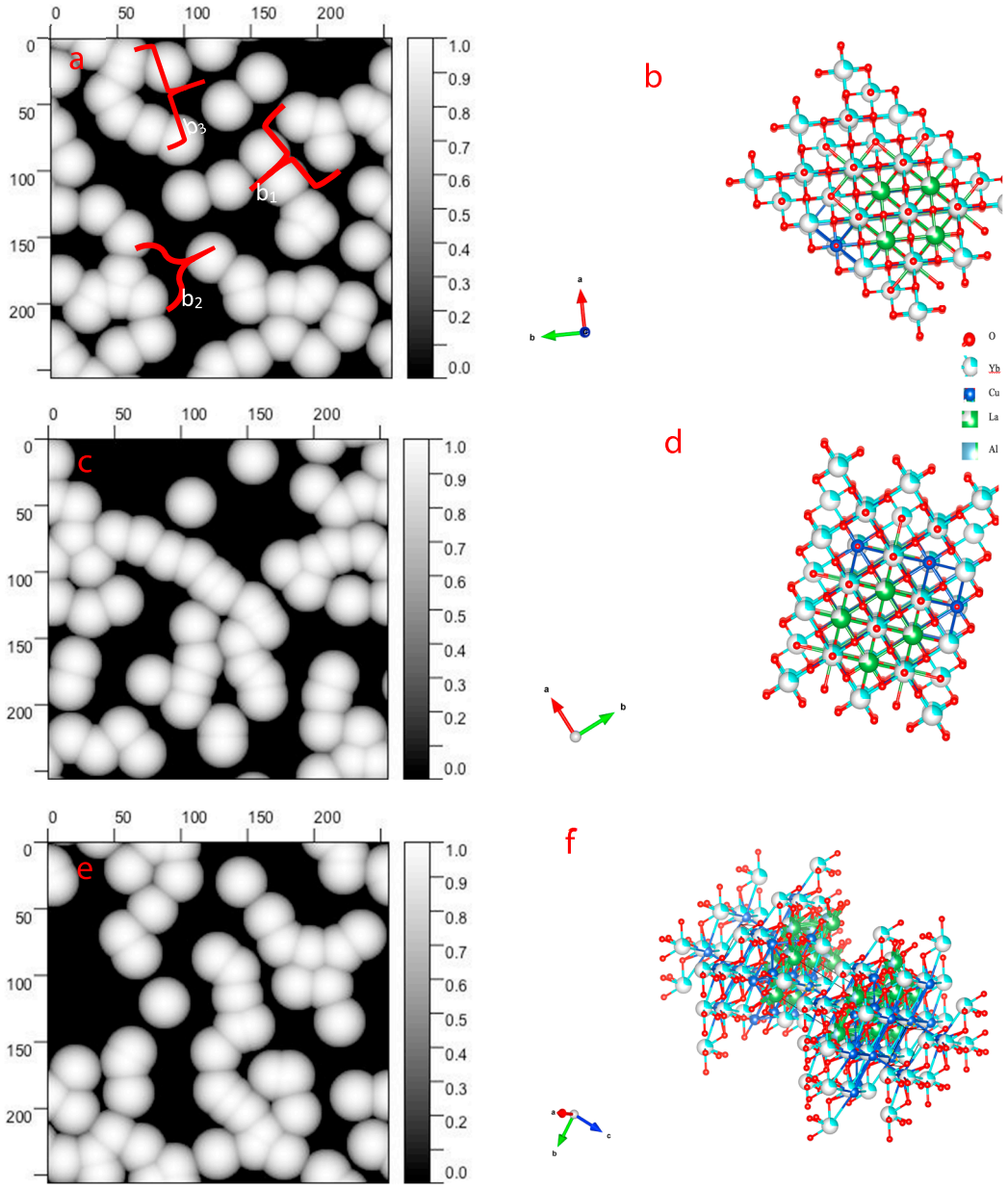

Fig. 5. Particulate displacement and corresponding structure in the sample.

Table 5
Selected Interatomic Distances (Å).

No	Elem.	Elem.	x	y	z	Occ.	Site	Sym.
1	La	La1	0.00000	0.00000	0.30000	0.500	1.000	4e
2	Al	Al1	0.00000	0.00000	0.30000	0.500	1.000	4e
3	La	La2	0.00000	0.00000	0.32170	0.750	1.000	4e
4	Yb	Yb1	0.00000	0.00000	0.12170	0.250	1.000	4e
5	Cu	Cu1	0.00000	0.00000	0.09130	1.000	1.000	4e
6	O	O1	0.00000	0.50000	0.18400	1.000	1.000	8g
7	O	O2	0.00000	0.00000	0.20500	1.000	1.000	4e
8	Cu	Cu2	0.00000	0.00000	0.19130	1.000	1.000	4e
9	Cu	O2	0.00000	0.00000	0.09130	1.000	1.000	4e
10	Cu	O1	0.00000	0.00000	0.09130	1.000	1.000	4e

charge reservoir.

The CuO_2 (Figs. 7–9) show that the dark regions along the b-axis correspond to missing atoms such as oxygen vacancy clusters along the CuO chain [27]. The dark regions are observed to be localized as previously discussed in Fig. 5 b, d & f. The statistics of the background (CuO_2 plane) is shown in Table 7 below. The distribution of the dark region of the background gives insight into the chemical homogeneity of the sample. For example, the skew and variation, entropy deficit and inclination angle in the whole sample (Table 7) is greater than the sections. This means that though the roughness varies at different sections, the collective significance on the whole sample is appreciably high. Hence, the polymorphic form of the new framework may be improved upon as its electronic properties.

Table 6
Selected Interatomic Bond Angles.

Element	a1	a2	a3	a4	a5	c	b1	b2	b3	b4	b5	bc
La:	19.966	27.330	11.018	3.087	17.335	−21.745	3.197	0.003	19.955	141.38	0.342	8.240
Cu:	14.014	4.785	5.057	1.458	6.933	−3.254	3.738	0.004	13.035	72.555	0.266	7.718
O:	2.960	2.509	0.638	0.723	1.143	0.027	14.182	5.937	0.113	34.958	0.390	5.803
Al:	4.731	2.314	1.542	1.118	3.155	0.140	3.629	43.051	0.096	108.93	1.556	3.449
Yb:	29.677	65.624	15.161	2.830	16.998	−60.314	1.978	0.001	11.045	108.13	0.192	12.430

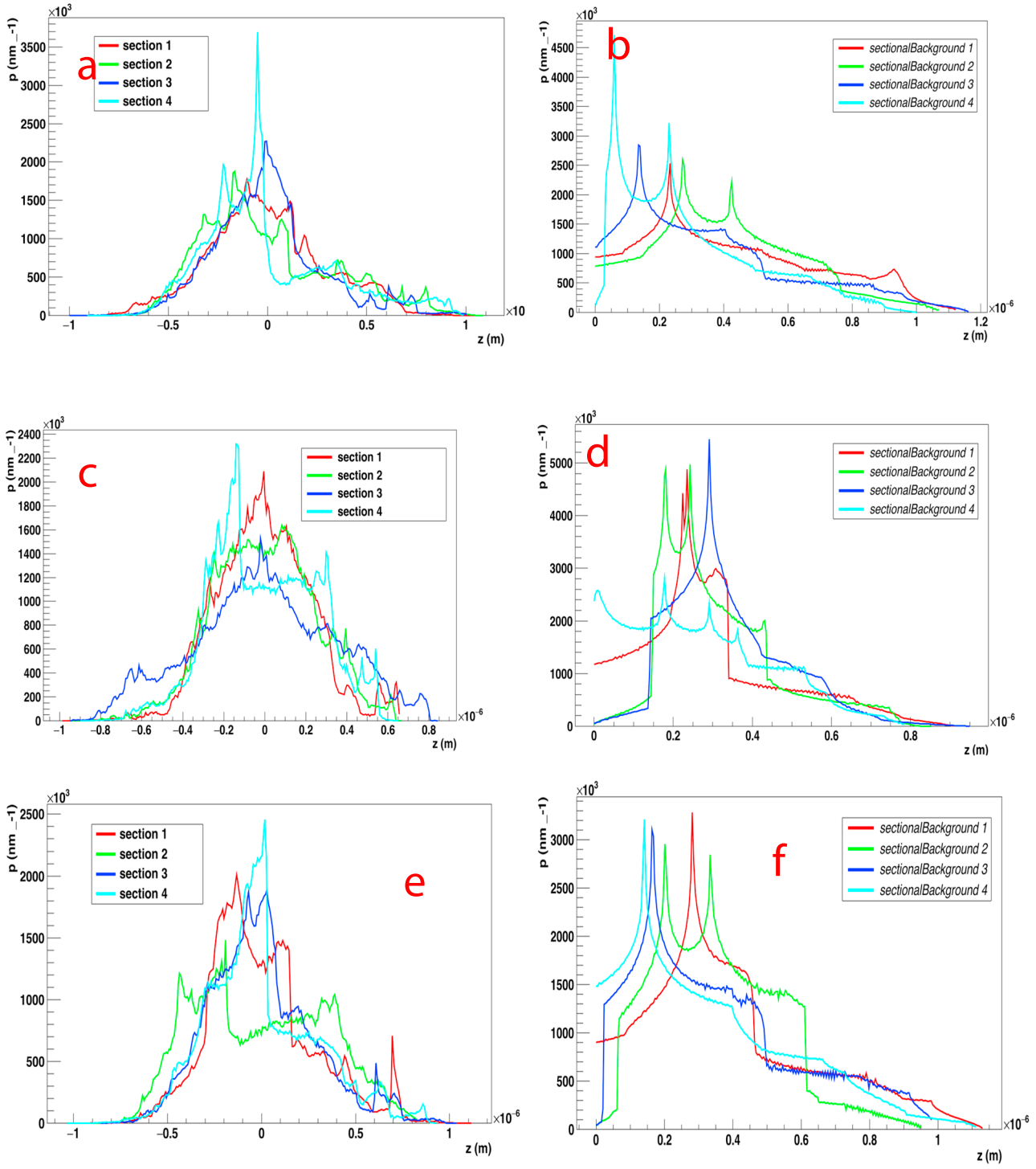

Fig. 6. Comparative analysis of interatomic distance and size in selected areas of SEM images.

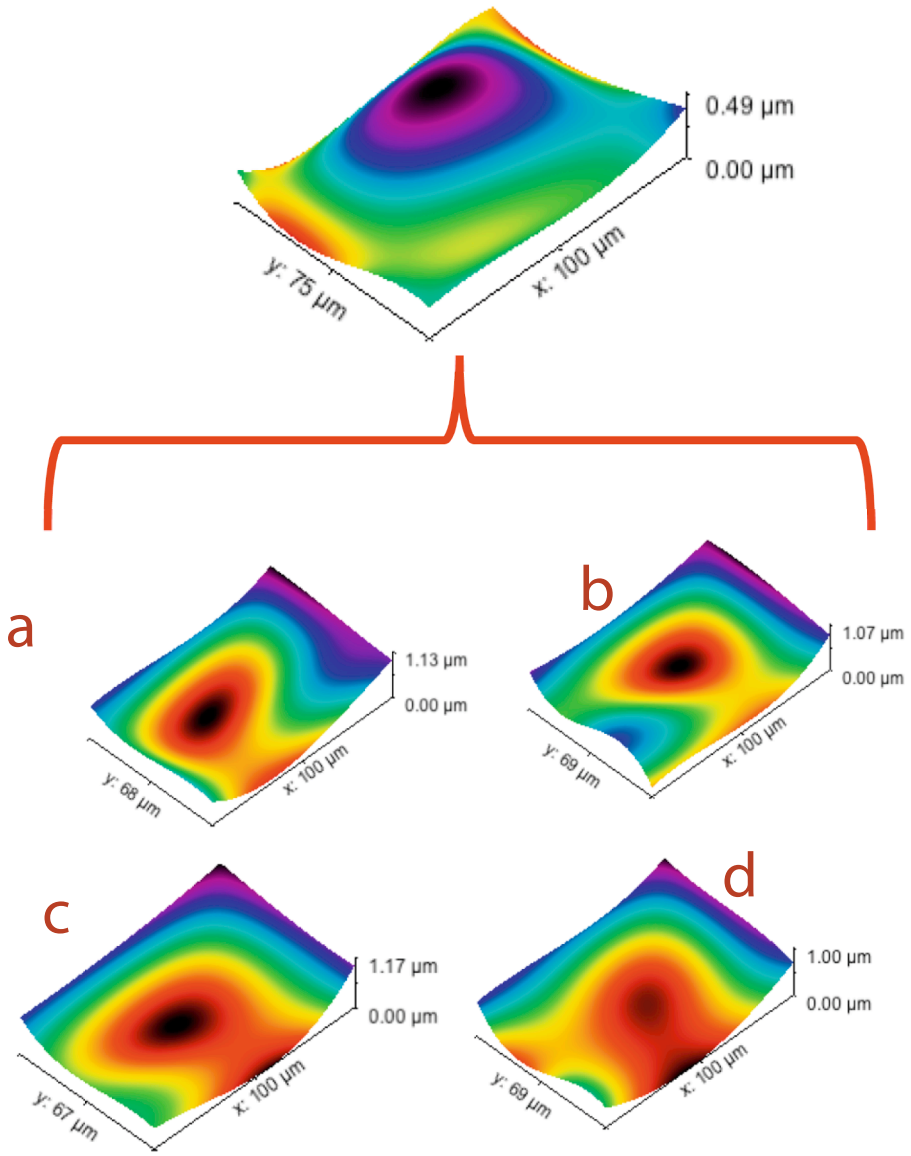

Fig. 7. CuO_2 plane variation at room temperature for image 1.

The orientation of the electrons in the compound may be better understood by the information on Tables 7–9. The inclination angles, as well as the entropy of the system show the kind of interaction, the estimated electronic specific heat coefficient and the number of carrier concentration that may be triggered when the phonon moves along the underlying lattice [28]. The entropy deficit in cuprates is largely due to applied thermal differentials but sometimes may be due to reduced carrier concentration in the transport measurements that has been initiated by pseudogap [29]. The entropy deficit shown in Tables 7–9 show that localized lattice structure may have significant influence on the entropy, as well as the electron transport in the sample. Hence, the dark region distributions in Figs. 7–9 may infer that the wide entropy deficit (structural modulation) within each localized lattice could uniquely drive the investigation positively or negatively depending on the characterizing equipment. In this study, the Rutherford Backscattering Spectrometry (RBS) was used to probe into the lattice modulation.

The inclination angles in Tables 7–9 corroborates the significance of structural modulation to experimental results. For example, the natural inclination angle (θ) of the whole sample presented in Tables 7–9 are 0.60°, 0.22° and 0.44° respectively. Assume the sample is placed on a goniometer of the probing device, the incident beam on the sample would have varying results on localized spots. Hence, structural faults or chemical composition may not be responsible for varying results on localized spots. The natural inclination of the atomic structure is quite important component interpretation.

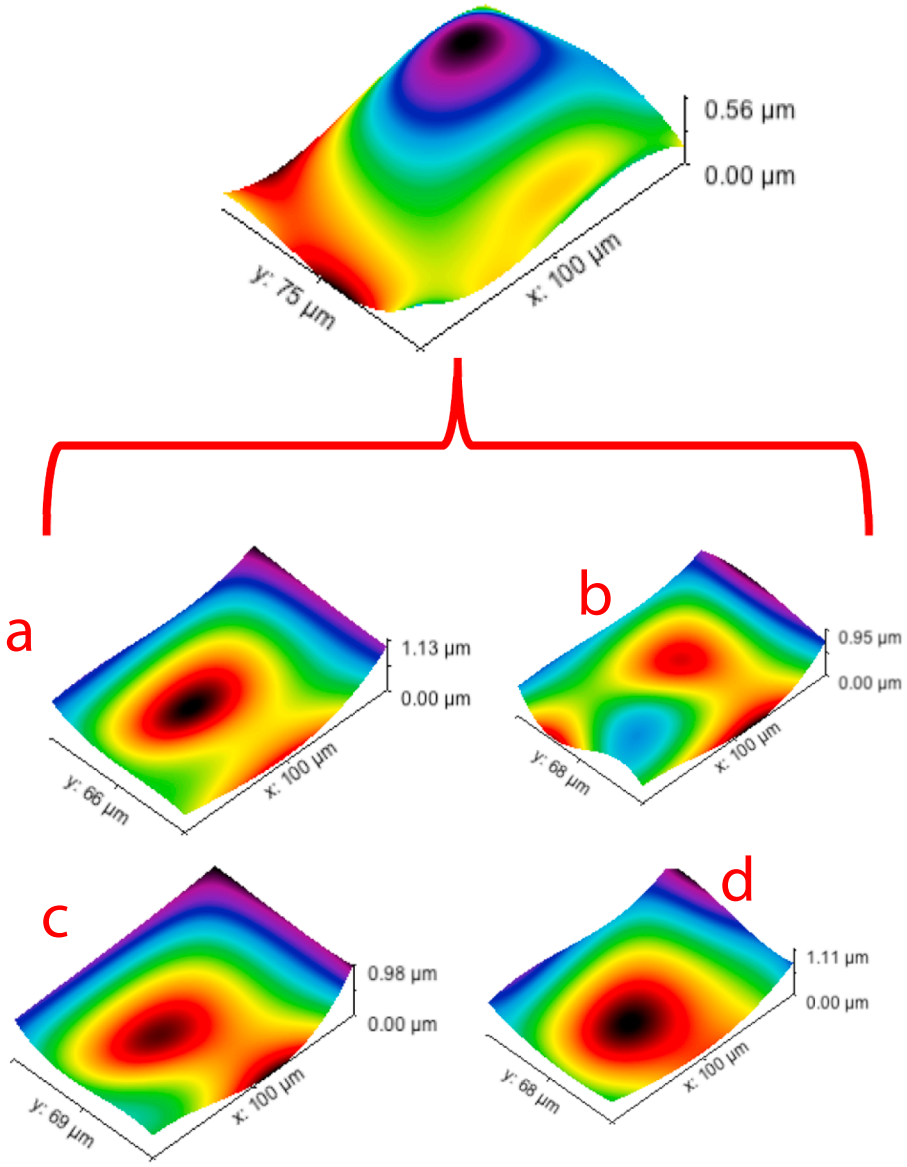

Fig. 8. CuO_2 plane variation at room temperature for image 2.

We investigate the potential of elastic scattering of energetic ions for compositional analysis of LAYbCO. The Rutherford Backscattering Spectrometry (RBS) set-up was made of 4He as the projectile ions with primary energies of 2 MeV. Elastic scattering techniques that was used yield information on the LAYbCO composition via scattering from the atomic nucleus. The advantages of 2.0 MeV RBS are clearly evident when examining the cation concentrations for La, Al, Yb and Cu in the surface and near surface region [30]. The SRIM software was used to show the estimate of the non-destructive depth profiling (Table 10).

As the number of the probing ions increased, the nuclear energy fluctuates within the depths of the LAYbCO pellet. Also, the electronic and nuclear properties fluctuate as the ion energy. The collective significance of the lateral position is further explained in Fig. 14. The result show that high Z elements are responsible for the consistent (near-linear) trend in LAYbCO. The atomic direction (Table 10) confirms the possibility of overlap that is caused by the high yields of heavier elements [31].

The lateral distribution shown in Fig. 10 is uniquely scanty. Only seven strand of information is provided for projected and radial straggling. The scanty strand of information can be explained using the ion distribution that is presented in Fig. 11. It is unclear if the peaks of the ion distribution signify the formation of diatomic negative-U centers (NUCs) proposed in ref [32]. The energy profile (i.e. displacement energy, lattice binding energy and surface binding energy) on the individual component was examined as shown in Table 11. The displacement energy (which refers to the minimum kinetic energy that an

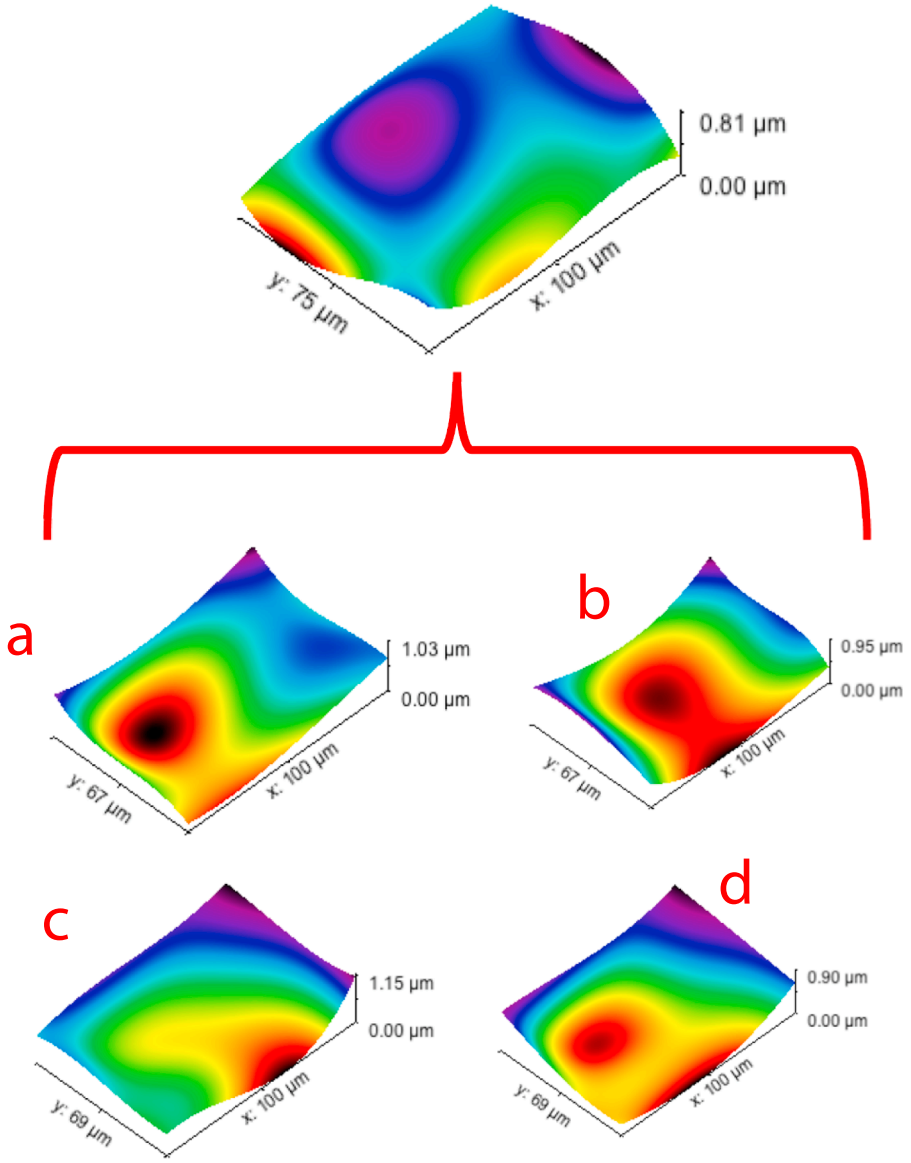

Fig. 9. CuO_2 plane variation at room temperature for image 3.

Table 7
Properties of the CuO_2 plane for image 1.

Quantities	Whole sample	Sample-side A	Sample-side B	Sample-side C	Sample-side D
RMS roughness (nm)	242.3	289.759	329.008	268.421	326.876
RMS -grain-wise (nm)	242.3	289.759	329.008	268.421	326.876
Mean roughness (nm)	169.5	228.698	266.753	201.161	256.527
Skew	1.685	0.215173	0.652086	0.623667	0.833946
Maximum peak height (µm)	1.089	1.08340	1.09629	1.01188	0.99609
Maximum pit depth (µm)	0.370	0.95346	0.89977	0.99876	0.90867
Maximum height (µm)	1.459	2.03686	1.99606	2.01064	1.90476
Projected area (μm^2)	7500	6756.03	6885.91	6680.05	6868.28
Surface area (μm^2)	12097.0	8958.93	9458.82	8244.72	9553.67
Variation (μm^2)	7318.0	4018.81	4542.80	2993.74	4718.30
Inclination θ (deg)	0.60	0.17	0.23	0.29	0.13
Inclination φ (deg)	−110.80	−74.10	−18.64	32.33	−13.74
Entropy	−14.18	−13.6630	−13.6070	−13.7782	−13.6859
Entropy deficit	0.3610	0.00277	0.0987786	0.0664802	0.171171

Table 8
Properties of the CuO_2 plane for image 2.

Quantities	Whole sample	Sample-side A	Sample-side B	Sample-side C	Sample-side D
RMS roughness (nm)	251.947	274.198	347.491	275.490	285.467
RMS -grain-wise (nm)	251.947	274.198	347.491	275.490	285.467
Mean roughness (nm)	211.477	215.853	300.573	213.806	220.936
Skew	0.375692	0.597067	0.150767	0.520303	0.495132
Maximum peak height (μm)	0.676440	1.12371	0.83761	1.04439	0.93636
Maximum pit depth (μm)	0.323560	0.93083	0.92637	0.86025	1.03230
Maximum height (μm)	1.000000	2.05454	1.76398	1.90464	1.96866
Projected area (μm^2)	7500	6595.17	6787.6	6904.44	6836.46
Surface area (μm^2)	11702.7	7977.69	10006.7	8682.41	9197.79
Variation (μm^2)	8171.92	2658.48	6062.25	3610.72	4478.92
Inclination θ (deg)	0.22	0.24	0.51	0.27	0.08
Inclination φ (deg)	119.92	22.73	−65.79	15.00	5.17
Entropy	−14.1684	−13.7673	−13.5406	−13.7311	−13.7226
Entropy deficit	0.393296	0.0767794	0.0870039	0.0452912	0.0724442

Table 9
Properties of the CuO_2 plane for image 3.

Quantities	Whole sample	Sample-side A	Sample-side B	Sample-side C	Sample-side D
RMS roughness (nm)	285.30	308.816	323.178	271.176	304.608
RMS -grain-wise (nm)	285.30	308.816	323.178	271.176	304.608
Mean roughness (nm)	233.80	259.004	272.643	214.471	254.047
Skew	0.4959	−0.187280	−0.132738	0.105536	0.307811
Maximum peak height (μm)	1.097	0.87540	0.79342	1.03255	0.91967
Maximum pit depth (μm)	0.655	0.92991	1.04754	0.98049	0.90835
Maximum height (μm)	1.7520	1.80532	1.84096	2.01303	1.82802
Projected area (μm^2)	7500	6720.43	6657.68	6885.91	6908.60
Surface area (μm^2)	13007.00	9186.37	9478.86	9068.25	9633.82
Variation (μm^2)	9670	5031.39	5547.79	4627.30	5341.94
Inclination θ (deg)	0.48	0.27	0.41	0.22	0.06
Inclination φ (deg)	−85.17	−91.01	−98.97	2.50	79.91
Entropy	−13.72	−13.6401	−13.5750	−13.7196	−13.6853
Entropy deficit	0.06497	0.0685137	0.0488900	0.0018	0.0999849

Table 10
Estimate of non-destructive depth profiling.

Ion	Energy	Depth	Lateral-Position		Atom Direction		
Num	(eV)	X (A)	Y(A)	Z(A)	Cos(x)	Cos (y)	Cos (z)
7690	1.46E+06	−2.52E+01	−4.66E+03	−8.06E+03	−1.76E−01	−5.05E−01	−8.45E−01
9862	1.03E+06	−3.88E+01	−1.72E+03	1.29E+04	−4.05E−01	−1.50E−01	9.02E−01
10,986	7.56E+05	−5.61E+01	−2.28E+03	1.76E+04	−4.78E−01	−8.97E−02	8.74E−01
11,559	1.22E+06	−3.90E+01	−5.11E+03	−1.66E+03	−5.95E−01	−7.62E−01	−2.58E−01
14,703	1.24E+06	−3.48E+01	5.37E+03	2.09E+03	−5.22E−01	7.91E−01	3.18E−01
17,014	1.24E+06	−3.76E−01	−3.34E+03	−4.89E+03	−6.96E−01	−3.87E−01	−6.05E−01
18,692	2.43E+05	−6.17E+01	−1.33E+04	−2.15E+04	−3.70E−01	−6.20E−01	−6.92E−01
44,096	4.40E+05	−2.66E+01	−7.96E+03	−2.45E+04	−1.73E−01	−3.31E−01	−9.28E−01
57,218	1.49E+05	−4.13E+01	−2.01E+04	−2.00E+04	−4.54E−01	−6.66E−01	−5.91E−01
61,859	1.56E+06	−3.48E+01	1.05E+03	−5.23E+03	−3.98E−01	1.66E−01	−9.02E−01
72,012	1.29E+06	−2.27E+01	3.61E+03	7.09E+03	−5.72E−01	3.61E−01	7.37E−01
74,801	1.41E+06	−6.60E+01	3.51E+02	3.42E+03	−7.55E−01	9.70E−02	6.48E−01
75,155	1.26E+06	−5.57E+01	2.67E+03	−3.86E+03	−8.23E−01	3.43E−01	−4.52E−01
75,721	1.42E+06	−1.61E+01	−6.29E+03	3.35E+03	−4.39E−01	−7.97E−01	4.16E−01
76,949	7.77E+05	−8.06E−01	1.22E+04	1.54E+04	−2.89E−01	6.44E−01	7.08E−01
78,263	7.37E+05	−1.39E+01	−9.44E+03	−6.34E+03	−6.93E−01	−6.24E−01	−3.61E−01
94,970	1.09E+06	−6.12E+01	−5.44E+03	−8.28E+03	−5.68E−01	−4.60E−01	−6.83E−01
99,249	1.08E+06	−9.64E+00	−8.94E+03	8.98E+03	−3.73E−01	−6.55E−01	6.57E−01
99,571	8.26E+05	−8.19E+01	−2.33E+03	1.03E+04	−5.90E−01	−1.98E−01	7.83E−01

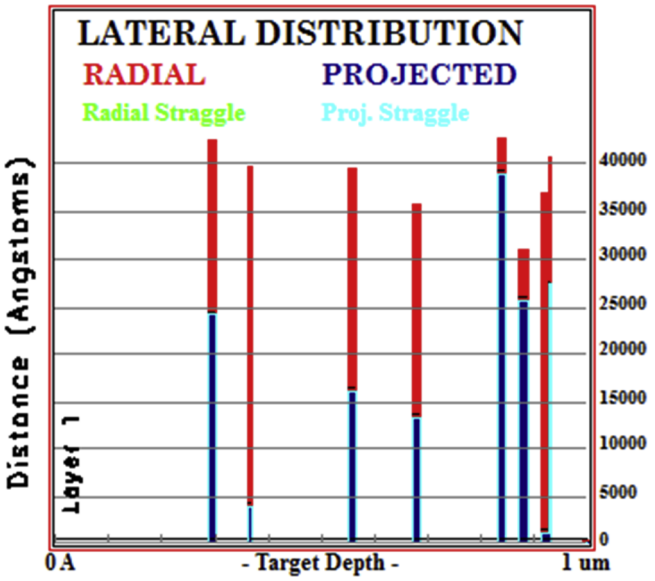

Fig. 10. The radial and projectile straggling within LAYbCO sample.

Table 11
Energy profile of the individual component of LAYbCO.

Element	Displacement Energy (ev)	Latt. Binding Energy (eV)	Surface Binding Energy (eV)
La	25.00	3.00	4.42
Al	25.00	3.00	3.36
Yb	25.00	3.00	1.74
Cu	25.00	3.00	3.52
O	28.00	3.00	2.00

atom in a solid need to be permanently displaced from its lattice site to a defect position) of La, Al, Yb and Cu is similar. This means that the peaks and strand of information (shown in Figs. 11 and 10) are evidence of interaction of electrons from oxygen band with the NUC's on pairs of Cu ions in CuO2 plane. However, it is still unclear if the NUC's are actually responsible for the superconducting pairing as proposed by ref [32]. La and Cu cations have the highest surface binding energy. Yb

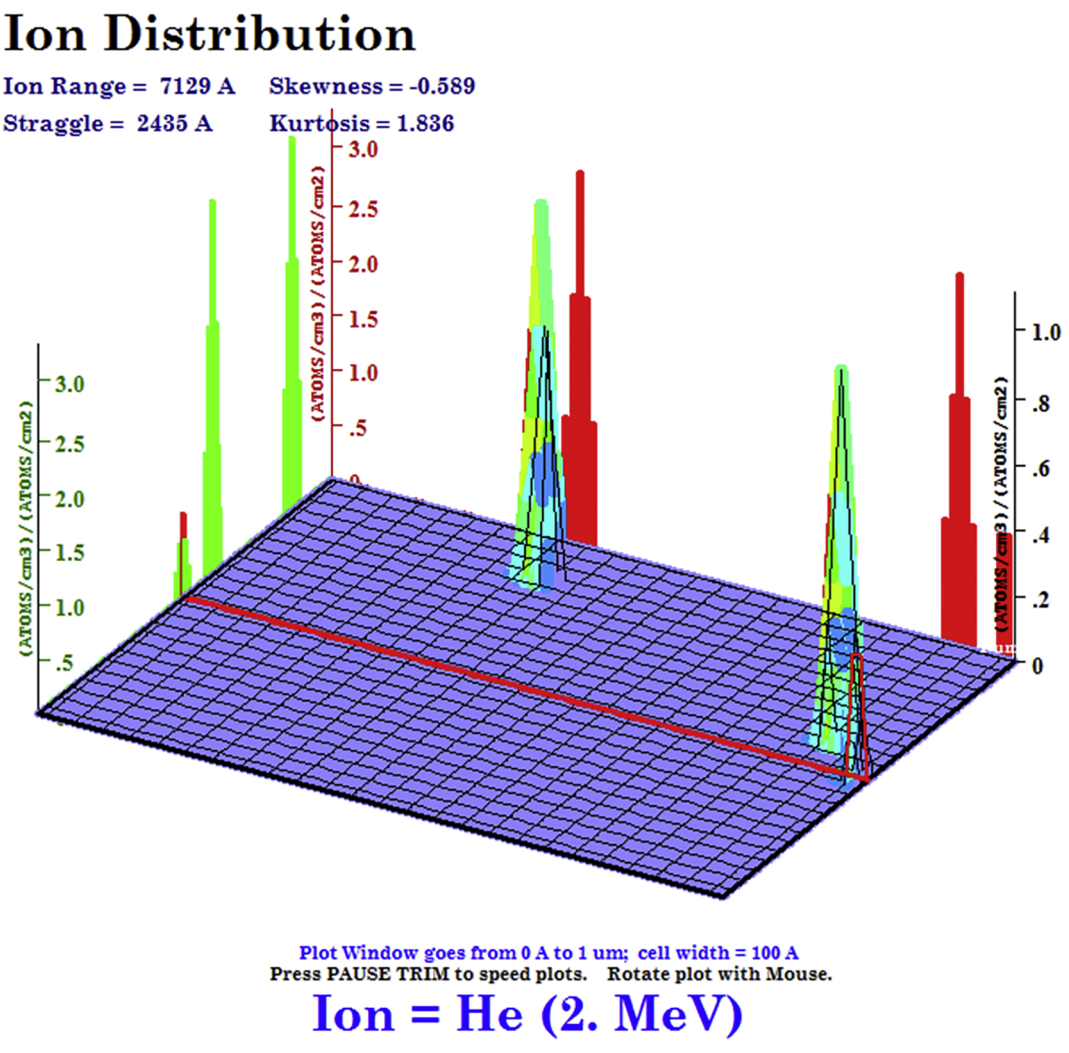

Fig. 11. Ion distribution within LAYbCO sample.

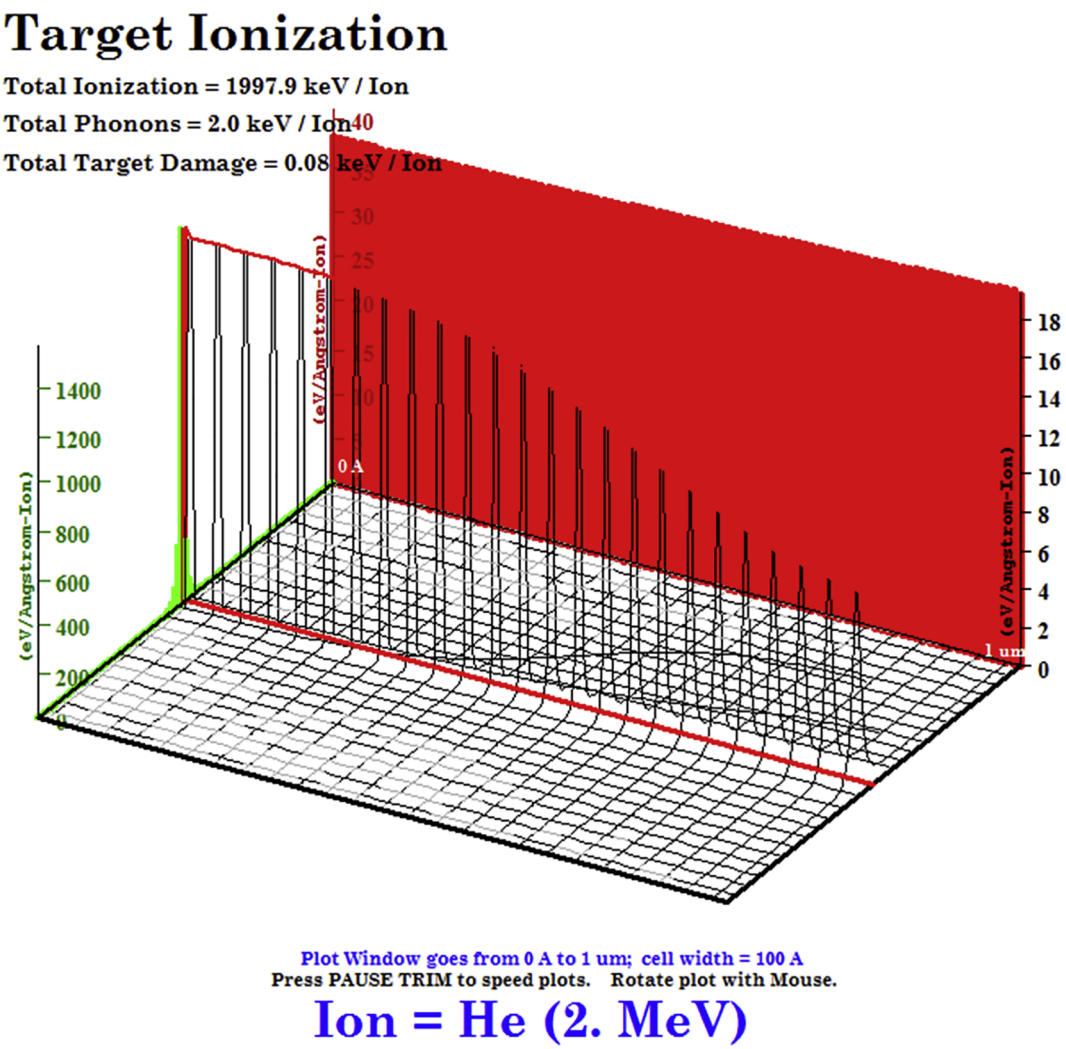

Fig. 12. The target ionization information within LAYbCO sample.

has the lowest surface binding energy.

The target ionization information within LAYbCO sample gives the total ionization as 1997.9 keV/Ion. The total phonon and target damage within the sample is given as 2 keV/Ion and 0.08 keV/Ion respectively. This part makes it easier to understand the extent of electron-phonon interaction in the LAYbCO sample. First, the ratio of electron to phonon production is approximately 999:1. These results make it clear that the electron-phonon may not really be a dominant factor for pairing. However, a close-look on the corresponding target ionization (Fig. 12) and phonon (Fig. 13) reveals that the massive ionization may likely be driven in its background by a subtle modulating phonon. Also, the phase transformation reported in ref [2] may be significant to initiate electron-phonon interaction within the sample. The possibility of pairing was described by the relationship between: counts in the lateral straggling and projected range (Fig. 14a); counts in the longitudinal straggling and projected range (Fig. 14b); counts in the longitudinal straggling and counts in the lateral straggling (Fig. 14c). There are two scenarios that can be observed in Fig. 14. First, the structure modulation may limit the electron-phonon interaction that initiates pairing. In this case, the electron-phonon interaction strictly depends on the lattice structure of the LAYbCO sample. Second, the electronic transport may be linearized by the structural modulation.

The RBS spectrum showing the identification of elements with respect to their documented energy levels is presented in Fig. 15. The closeness of heavy Z element is clearly shown by the counts per channel. The fitting of the RBS spectrum was done using parameters like Cal A, Cal B, Beam energy, detector FWHM, Beam-det angle, in-plane tilt angle, out-of-plane tilt angle, straggling, pile-up and constant background on the OMDAQ software. The compositional ratios of the element where determined through the fits (Fig. 16). The compositional analysis of LAYbCO, that is, based on various OMDAQ parameters is shown in Table 12. When no parameter was used for the fitting, the

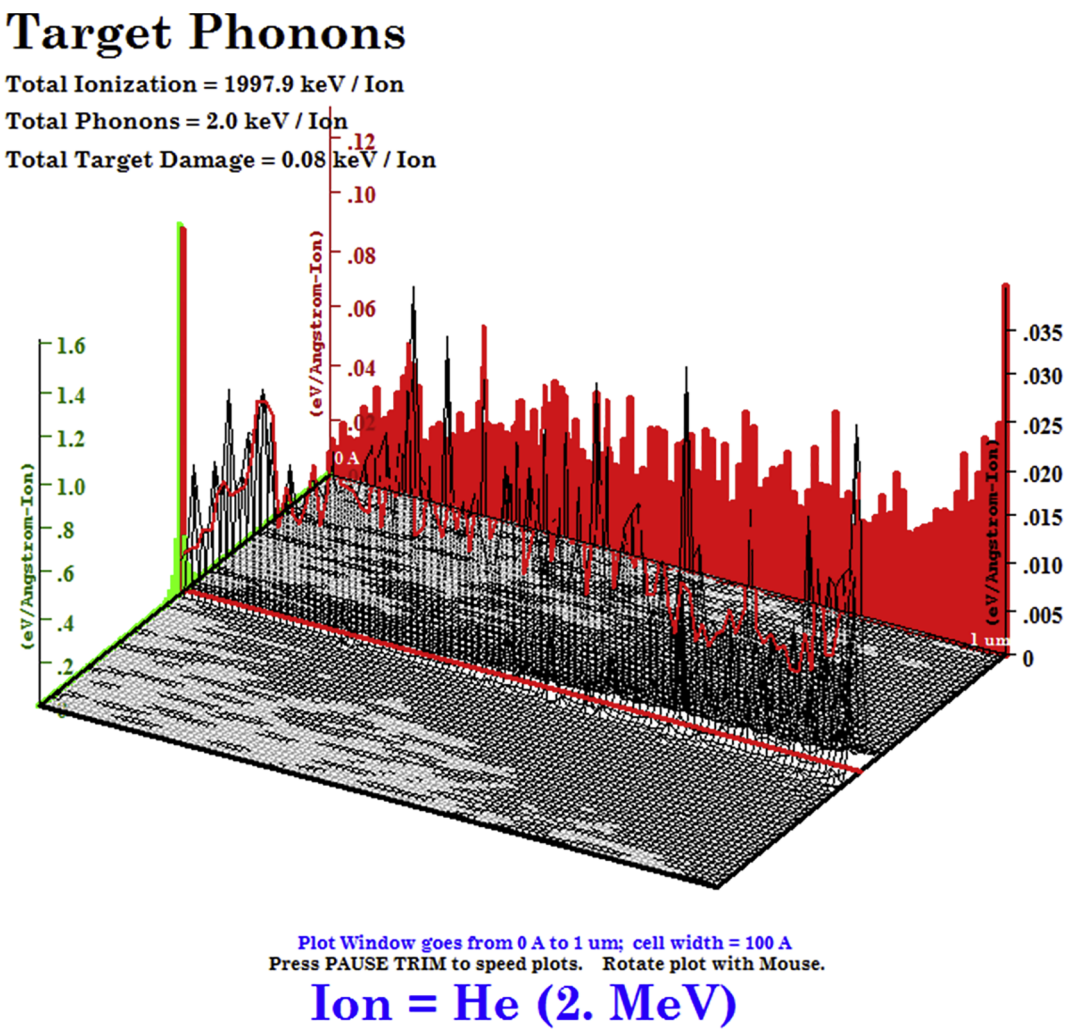

Fig. 13. The target phonon information within LAYbCO sample.

LAYbCO composition was $La_{0.05}Al_{2.05}Yb_{4.64}Cu_{2.81}O_{15}$ at Q-factor – 0.033, Chi-square – 0.8180 and dMax – 158. Also, when all of the parameters listed in Table 12 were used to plot the fit, the elemental composition of LAYbCO is given as $La_{1.35}Al_{3.97}$ $Yb_{6.80}Cu_{6.80}O_{15}$ at Q-factor – 0.033, Chi-square – 0.6057 and dMax – 173.

Conclusion

The XRD refinements show that LAYbCO has orthorhombic structure with unit cell as a = 3.865 Å, b = 3.865 Å, c = 19.887 Å. 62.9% of the peaks were seen to correspond to existing database while the unidentified peak is 37.1%. The unidentified peaks show the newness of the proposed lanthanum cuprates framework. The internal atomic structure inclination of LAYbCO was found to significantly affect spot characterization. The O(1) and O(2) of the LAYbCO lie in the Wyckoff positions 4e and 8 g which gives a vintage point to initialize NUC's within the LAYbCO framework.

From the RBS spectrum it was observed that the ratio of electron to phonon production is approximately 999:1. Though the electron-phonon ratio may be low, it does not strike-out the possibility of phonon-electron interaction due to phase transformation that is peculiar to the lanthanum superconductor. The elemental composition of LAYbCO is given as $La_{1.35}Al_{3.97}$ $Yb_{6.80}Cu_{6.80}O_{15}$ at Q-factor – 0.033, Chi-square – 0.6057 and dMax – 173. It was experimentally proven that CuO_2 plane plays a salient role in local lattice fluctuation and atomic-scale mechanism in LAYbCO at room temperature. However, it was also reported that the influence of the CuO plane is not very significant structurally despite the chemical homogeneity of the LAYbCO framework. In conclusion, the new LAYbCO high temperature superconductor seem to be more rugged with higher prospects for engineering application. More study is recommended to understand the transport properties of LAYbCO.

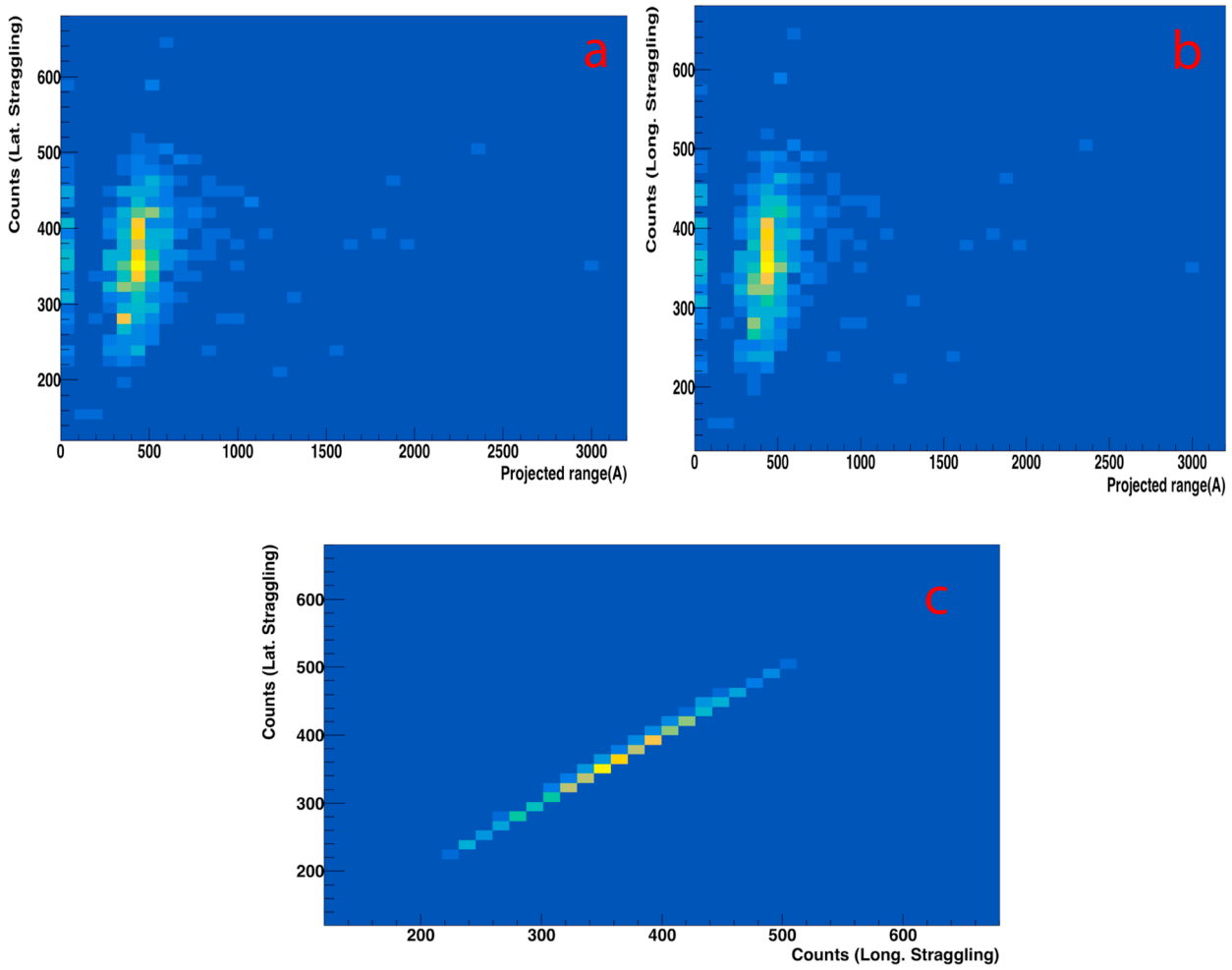

Fig. 14. Path description of electron-phonon triggered electronic transport.

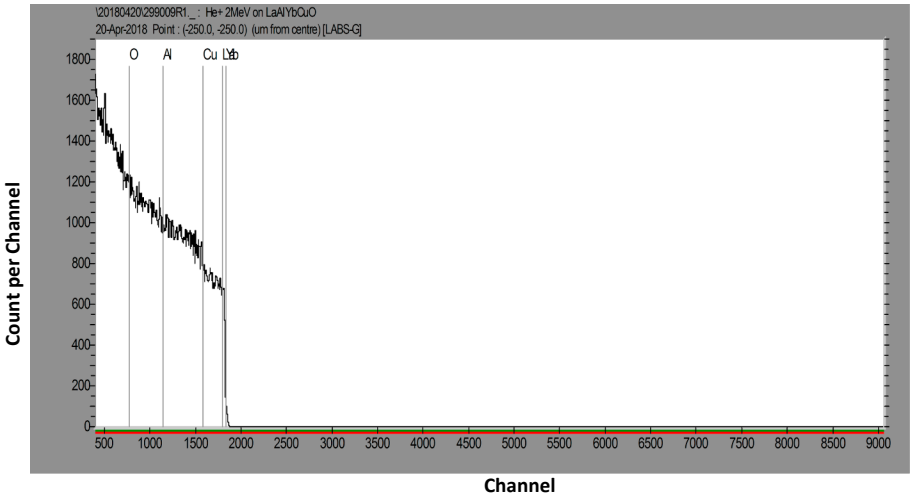

Fig. 15. RBS spectrum.

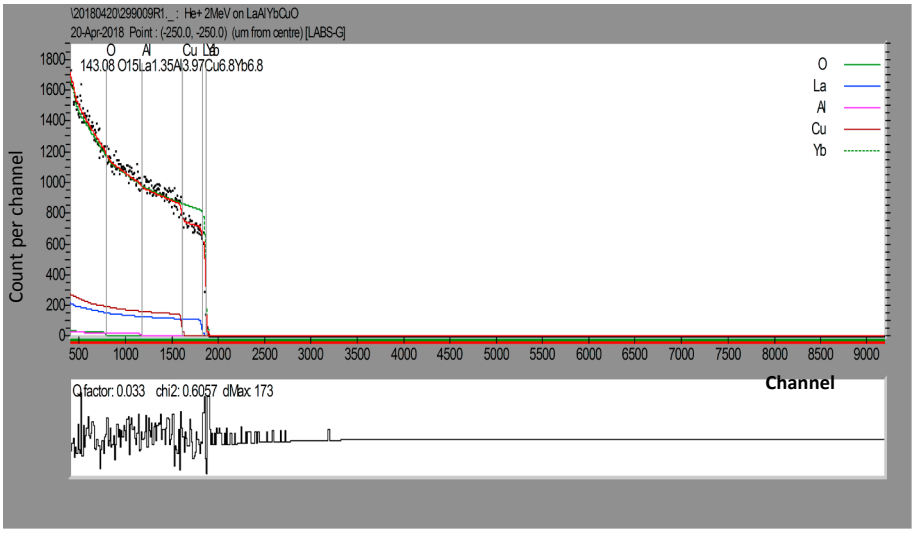

Fig. 16. Compositional analysis of RBS spectrum using OMDAQ.

Table 12
Compositional analysis of LAYbCO.

Description	O	La	Al	Yb	Cu	Q-factor	Chi2	dMax
Nothing	15.00	0.05	2.05	4.64	2.81	0.033	0.8180	158.0
Cal A	15.00	0.49	4.25	5.21	3.32	0.033	0.7907	160.0
Cal B	15.00	1.78	6.42	6.67	3.83	0.030	0.6745	135.0
Beam energy + Cal B	15.00	1.75	6.23	6.66	3.87	0.030	0.6737	134.0
Beam energy	15.00	1.78	6.38	6.67	3.83	0.030	0.6742	135.0
detector FWHM	15.00	1.75	6.14	6.45	3.90	0.031	0.6775	135.0
Beam-Det angle [phi]	15.00	2.19	5.67	6.14	4.72	0.031	0.6579	139.0
In-plane tilt angle	15.00	2.11	5.72	4.81	5.21	0.036	0.6387	170.0
out-of-plane tilt angle	15.00	2.16	5.80	6.92	6.59	0.032	0.6240	157.0
Straggling	15.00	1.68	4.54	6.70	6.88	0.032	0.6184	155.0
Pile-up	15.00	1.70	4.57	6.75	6.87	0.032	0.6186	153.0
constant Background	15.00	1.72	4.37	6.65	6.76	0.032	0.6185	155.0
All	15.00	1.35	3.97	6.80	6.80	0.033	0.6057	173.0

Acknowledgement

The authors wish to acknowledge the above-listed institutions. The authors declare no competitive interest. The authors contributed equally.

Additional information

The authors declare no competitive interest.

Appendix A. Supplementary data

Supplementary data to this article can be found online at https://doi.org/10.1016/j.rinp.2019.01.058.

References

[1] Axe JD, Crawford MK. Structural instabilities in lanthanum cuprate superconductors. J Low Temp Phys 1994;95:271–84.
[2] Bagcı S, Tutuncu HMT, Duman S, Srivastava GP. Phonons and superconductivity in fcc and dhcp lanthanum. Phys Rev B 2010;81:144507.
[3] Birgeneau RJ, Chen CY, Gabbe DR, Jenssen HP, Kastner MA, Peters CJ, et al. Soft-phonon behavior and transport in single-crystal La 2 CuO 4. Phys Rev Lett 1987;59:1329.
[4] Buzea Cristina, Robbie Kevin. Assembling the puzzle of superconducting elements: a Review. Supercond Sci Technol 2005;18:R1–8.
[5] Liu Hanyu, Naumov Ivan I, Hoffmann Roald, Ashcroft NW, Hemley Russell J. Potential high-Tc superconducting lanthanum and yttrium hydrides at high pressure. PNAS 2017;114(27):6990–5.
[6] Moshchalkov VV, Gielen L, Neuttiens G, Van Haesendonck C, Bruynseraede Y. Intrinsic resistance fluctuations in mesoscopic superconducting wires. Phys. Rev. B 1994;49:15412–5.
[7] McMahan K, Young DA. Is there a missing rare earth crystal structure? Phys Lett A 1984;105:129–31.
[8] Baiutti F, Wrobel F, Christiani G, Logvenov G. Oxide molecular beam epitaxy of complex oxide heterointerfaces. Metal Oxide-Based Thin Film Structures 2018:53–78.
[9] Crawford MK, Harlow RL, Deemyad S, Tissen V, Schilling JS, McCarron EM, et al. High-pressure study of structural phase transitions and superconductivity in La1.48Nd0.4Sr0.12CuO4. Phys. Rev. B 2005;71:104513.
[10] Aoki Hideo, Hosono Hideo. A superconducting surprise comes of age. Phys World 2015;28(2):31–6.
[11] Schirber JE, Morosin B, Merrill RM, Hilava PF, Venturinie L, Kwak JF, et al. A superconducting superoxide? Physica C 1988;152(1):121–3.
[12] Drozdov AP, Minkov VS, Besedin SP, Kong PP, Kuzovnikov MA, Knyazev DA, Eremets MI. Superconductivity at 215 K in lanthanum hydride at high pressures. ArXiv180807039 Cond-Mat 2018.
[13] Bednorz JG, Müller KA. Possible high Tc superconductivity in the Ba-La-Cu-O system. Z Phys B: Condens Matter 1986;64(2):189–93.
[14] Barisic S, Tutis E. Effect of strong electron correlations on the electron-phonon coupling in high Tc superconductors. Sol St Commun 1993;87:557–61.
[15] Mazaheri M, Jamas S. Electrical transport in the superconducting and normal states in $Y_2Ba_5Cu_7O_x$ high-temperature superconductor. Solid State Commun 2016;234–235:21–5.
[16] Nishizaki Terukazu, Shibata Kenji, Maki Makoto, Kobayashi Norio. STM/STS studies on vortex and electronic state in YBa2Cu3Oy. Physica C 2006;437–438:220–5.
[17] Božin ES, Huq A, Shen B, Claus H, Kwok WK, Tranquada JM. Charge-Screening Role of c-Axis Atomic Displacements in YBa2Cu3O6þx and Related Superconductors. Phys. Rev. B 2016;93:054523.
[18] Hostachy A, Coing Boyat J. Structure cristalline de Cu3 Te O6, Comptes Rendus Hebdomadaires des Seances de l'Academie des Sciences. Serie B 1968;267:14351438.
[19] Poltavets Viktor V, Lokshin Konstantin A, Mark Croft, Mandal Tapas K, Takeshi Egami, Martha Greenblatt. Crystal structures of Ln4Ni3O8 (Ln = La, Nd) triple layer T'typenickelates. Inorg Chem 2007;46(25):10887–91.
[20] Marezio M, Remeika JP. High pressure synthesis and crystal structure of alphaLiAlO2. J Chem Phys 1966;44:3143–4.
[21] Iandelli A, Palenzona A. Das Verhalten des Ytterbiums mit den Metallen der achten Gruppe desperiodischen Systems. Revue de Chimie Minerale 1976;13:5561.
[22] Attfield JP, Kharlanov AL, McAllister JA. Cation effects in doped La2CuO4 superconductors. Nature 1998;394:157.
[23] Locquet JP, Perret J, Fompeyrine J, Machler E, Seo JW, Van Tendelloo G. Doubling the critical temperature of La1.9Sr0.1CuO4 using epitaxial strain. Nature 1998;394:453.
[24] McElroy K, Lee Jinho, Slezak JA, Lee D-H, Eisaki H, Uchida S, Davis JC. Atomic-scale sources and mechanism of nanoscale electronic disorder in Bi2Sr2CaCu2O8. Science 2005;309:1048–52.
[25] Dadras S, Dehghani S, Davoudiniya M, Falahati S. Improving superconducting properties of YBCO high temperature superconductor by Graphene Oxide doping. Mater Chem Phys 2017;193:496–500.
[26] az Hadi-Sichani, Shakeripour Hamideh, Salamati Hadi. Structural investigation of $Y_{1-x}Ni_xBa_2Cu_3O_{7-\delta}$ superconductor. Physica C (Amsterdam, Neth) 2018;550:92–4.
[27] Rybicki Damian, Jurkutat Michael, Reichardt Steven, Kapusta Czesław, Haase

Jurgen. Perspective on the phase diagram of cuprate high-temperature superconductors. Nat Commun 2016;7:1141.
[28] Storey JG. Incoherent superconductivity well above Tc in high-Tc cuprates harmonizing the spectroscopic and thermodynamic data. New J Phys 2017;19:073026.
[29] Waldram JR. 1996. Superconductivity of Metals and Cuprates, 1st Edition, IOP publishing limited, pg 263 ISBN-10: 0852743378.
[30] Martin Jarrod W, Russell Greame J. Selective Rutherford Backscattering Techniques in the Study of Transition-Metal Implanted YBa2Cu3O74. Aust Conf Nucl Techn Anal 1993:168–70.
[31] Roumie M, Awad R, Ibrahim IH, Zein A, Zahraman K, Nsouli B. PIXE and RBS analysis of Tl-1223 superconducting phase substituted by scandium. Nucl Instrum Methods Phys Res B 2008;266:133–9.
[32] Mitsen KV, Ivanenko OM. Possible nature of the pseudogap anomalies in HTSC. JETP 2008;107:984–95.